Surface-Wave Attenuation From Seismic Ambient Noise: Numerical Validation and Application

Fabrizio Magrini, Lapo Boschi

JGR Solid Earth

RESEARCH ARTICLE
10.1029/2020JB019865

Surface-Wave Attenuation From Seismic Ambient Noise: Numerical Validation and Application

Fabrizio Magrini[1] and **Lapo Boschi**[2,3,4]

[1]Department of Sciences, Università Degli Studi Roma Tre, Roma RM, Italy, [2]Dipartimento di Geoscienze, Università Degli Studi Di Padova, Padova, Italy, [3]Sorbonne Université, CNRS, INSU, Institut des Sciences de La Terre De Paris, Paris, France, [4]Istituto Nazionale Di Geofisica e Vulcanologia, Bologna, Italy

Key Points:

- Synthetic data are generated, to validate inverse theory relating seismic ambient noise and surface-wave attenuation
- Inversion of synthetic data suggests that ambient noise, even when not perfectly "diffuse," is a useful constraint to attenuation
- Preliminary application to North American data yields attenuation estimates compatible with previous studies

Supporting Information:

- Supporting information S1

Correspondence to:
F. Magrini,
fabrizio.magrini@uniroma3.it

Citation:
Magrini, F., & Boschi, L. (2021). Surface-wave attenuation from seismic ambient noise: numerical validation and application. *Journal of Geophysical Research: Solid Earth*, *126*, e2020JB019865. https://doi.org/10.1029/2020JB019865

Received 1 APR 2020
Accepted 27 NOV 2020

Abstract We evaluate, by numerical tests, whether surface-wave attenuation can be determined from ambient-noise data. We generate synthetic recordings of numerically simulated ambient seismic noise in several experimental setups, characterized by different source distributions and different values of attenuation coefficient. We use them to verify that the source spectrum can be reconstructed from ambient recordings (provided that the density of sources and the attenuation coefficient are known) and that true attenuation can be retrieved from normalized cross correlations of synthetic signals. We then apply the so validated method to real continuous recordings from 33 broadband receivers distributed within the Colorado Plateau and Great Basin. A preliminary analysis of the signal-to-noise ratio as a function of azimuth reveals a SW-NE preferential directionality of the noise sources within the secondary microseism band (6–8 s), consistent with previous studies. By nonlinear inversion of noise data we find the attenuation coefficient in the area of interest to range from $\sim 1 \times 10^{-5}$ m^{-1} at 0.3 Hz to $\sim 4.5 \times 10^{-7}$ m^{-1} at 0.065 Hz, and confirm the statistical robustness of this estimate by means of a bootstrap analysis. The result is compatible with previous observations based on both earthquake-generated and ambient Rayleigh waves. In this regard, the method proves to be promising in accurately quantifying surface-wave attenuation at relatively high frequencies.

1. Introduction

Over the last century, seismologists have learned to constrain the velocity of seismic waves increasingly well, but its interpretation in terms of temperature, density, viscosity, and composition of the Earth's interior is nonunique and remains problematic. As opposed to their speed of propagation, the *amplitude* of seismograms is directly related to anelastic dissipation; knowing how the Earth attenuates seismic waves, and how such attenuation changes with location within our planet, would tell us much more about its properties than we currently know. However, measures of amplitude carry important uncertainty, and the theory relating seismogram amplitude to Earth parameters is cumbersome and occasionally (e.g., Boschi et al., 2019; Menon et al., 2014) controversial.

Several studies have shown that cross correlations of seismic ambient noise approximately coincide with the surface-wave Green's function associated with the two points of observation. By analyzing the *phase* of the empirical Green's function, it is possible to successfully image and monitor the velocity structure of the Earth's interior (see the reviews by, e.g., Boschi & Weemstra, 2015; Campillo & Roux, 2014). The information on the anelastic properties carried by its *amplitude*, on the other hand, is less accurately reconstructed by cross correlation (e.g., Lehujeur & Chevrot, 2020). Initial attempts to constrain surface-wave attenuation from ambient noise (e.g., Lawrence & Prieto, 2011; Prieto et al., 2009) were based on the assumption that attenuation could be accounted for by simply taking the product of the Green's function and an exponential damping term. Tsai (2011) showed that these works omitted a multiplicative factor dependent on source parameters, which, if not accounted for, is likely to introduce a bias in the attenuation estimates; Weemstra et al. (2013) chose to treat that factor as a free parameter in their formulation of the inverse problem. However, Weemstra et al. (2014) showed an additional difficulty associated with the normalization of cross correlations, used in ambient-noise literature to reduce the effects of, e.g., strong earthquakes; spectral whitening or other normalization terms affect the amplitude of the empirical Green's function, biasing the measurements of attenuation. Boschi et al. (2019) derived a mathematical expression for the multiplicative factor relating normalized cross correlations to the Rayleigh-wave Green's function; numerical evaluation

showed it to be equal to 1, under the assumption of a spatially uniform source distribution, confirming the speculation of Prieto et al. (2009).

It can be inferred from the mentioned theoretical contributions, as well as from that of Nakahara (2012), that—in an idealized situation (spatial and spectral uniformity of source distribution)—surface-wave attenuation can be measured from seismic ambient-noise data. The purpose of this study is to quantify the error that is caused, in such attenuation estimates, by applying the algorithm of Boschi et al. (2019, 2020) to recordings of nonidealized, more realistic seismic noise. We model those by numerical simulation of the signal resulting from a suite of increasingly non-uniform source distributions. We then invert the synthetic data and evaluate the similarity of the thus obtained attenuation estimates to the attenuation model used to compute the data.

Our inversion technique differs from those implemented by other authors in several aspects. First of all, we determine phase velocity through a preliminary, independent inversion: this is preferable to constraining velocity and attenuation at the same time, since phase velocity is directly related to the "zero crossings" of the Green's function in the frequency domain and independent of its amplitude (e.g., Boschi et al., 2013; Ekström et al., 2009). The so obtained velocity is then a fixed parameter of the attenuation inversion. Second, we do not average ambient-noise cross-correlation data over azimuth and/or distance, and we minimize the sum of misfits associated with each interstation pair. Earlier work by Menon et al. (2014), as well as the synthetic tests presented here, indicate that this contributes to "regularizing" the inversion, resulting in an apparently more accurate solution. Third, cross correlations are systematically processed in the time domain, prior to inversion, so as to remove any signal associated with surface-wave overtones.

The results of our numerical tests, discussed in Section 4, indicate that our approach can potentially contribute to constraining surface-wave attenuation at regional and continental scale, where Rayleigh-wave fundamental mode dominates the seismic ambient noise. A preliminary application to USArray is given in Section 5. The relative success of our tests both confirms the validity of the theory (summarized in Section 2) and shows that our inversion strategy (described in detail in Section 3) is sound.

2. Theory

2.1. Rayleigh-Wave Green's Function

Following, e.g., Tsai (2011) and Boschi et al. (2019), we assume that surface-wave attenuation can be accounted for by replacing the equation governing the displacement of a lossless, stretched membrane with that of a damped membrane equation. We define the 2-D Green's function as the membrane response to impulsive initial velocity generated at $\mathbf{x}_S$ and recorded at $\mathbf{x}$ (e.g., Boschi et al., 2019, Appendix A),

$$G_{2D}^{d}\left(\mathbf{x},\mathbf{x}_S,\omega\right) = -\frac{i}{4\sqrt{2\pi}c^2}H_0^{(2)}\left(\left|\mathbf{x}-\mathbf{x}_S\right|\sqrt{\frac{\omega^2}{c^2}-\frac{2i\alpha\omega}{c}}\right), \tag{1}$$

where i, ω, c, and α denote imaginary unit, angular frequency, phase velocity and attenuation coefficient, respectively; $|\mathbf{x}-\mathbf{x}_S|$ is the distance between the impulsive source and the receiver, and $H_0^{(2)}$ a zero-order Hankel function of the second kind. Equation 1 is equivalent to Equation 8 of Boschi et al. (2019), except for a constant factor—dubbed P by Boschi et al. (2019)—that served to keep track of the physical dimensions of G_{2D} and that is omitted here for simplicity. As shown by Boschi et al. (2019), provided that attenuation is relatively weak, i.e., $\alpha \ll \omega/c$, Equation 1 can be reduced to the more convenient, approximate form

$$G_{2D}^{d}\left(\mathbf{x},\mathbf{x}_S,\omega\right) \approx -\frac{i}{4\sqrt{2\pi}c^2}H_0^{(2)}\left(\frac{\omega\left|\mathbf{x}-\mathbf{x}_S\right|}{c}\right)\mathrm{e}^{-\alpha\left|\mathbf{x}-\mathbf{x}_S\right|}, \tag{2}$$

employed throughout this study.

2.2. Cross Correlation of Ambient-Noise Recordings

By the properties of the Green's function, a signal of amplitude $h(\omega)$ and phase ϕ emitted at $\mathbf{x}$ and recorded at $\mathbf{x}_A$ reads $h(\omega)G^d_{2D}(\mathbf{x}_A,\mathbf{x},\omega)e^{i\phi}$. The vertical-component, Rayleigh-wave displacement associated with a set of N_S sources with the same amplitude $h(\omega)$, but different phase, is then

$$s(\mathbf{x}_A,\omega) = h(\omega)\sum_{j=1}^{N_S} G^d_{2D}(\mathbf{x}_A,\mathbf{x}_j,\omega)e^{i\phi_j}, \tag{3}$$

where the index j identifies the source. Let a second receiver, located at $\mathbf{x}_B$, also record the signal emitted by the same sources. In the frequency domain, the cross correlation of recordings made at $\mathbf{x}_A$ and $\mathbf{x}_B$ is then given by

$$\begin{aligned} s(\mathbf{x}_A,\omega)s^*(\mathbf{x}_B,\omega) &= h^2(\omega)\left[\sum_{j=1}^{N_S} G^d_{2D}(\mathbf{x}_A,\mathbf{x}_j,\omega)e^{i\phi_j}\right]\left[\sum_{k=1}^{N_S} G^{d*}_{2D}(\mathbf{x}_B,\mathbf{x}_k,\omega)e^{-i\phi_k}\right] \\ &= h^2(\omega)\left[\sum_{j=1}^{N_S} G^d_{2D}(\mathbf{x}_A,\mathbf{x}_j,\omega)G^{d*}_{2D}(\mathbf{x}_B,\mathbf{x}_j,\omega)\right. \\ &\quad \left. + \sum_{j=1}^{N_S}\sum_{k=1,k\neq j}^{N_S} G^d_{2D}(\mathbf{x}_A,\mathbf{x}_j,\omega)G^{d*}_{2D}(\mathbf{x}_B,\mathbf{x}_k,\omega)e^{i(\phi_j-\phi_k)}\right] \end{aligned} \tag{4}$$

(e.g., Press et al., 1992, Section 13.2), where * denotes complex conjugation.

Seismic surface-wave ambient noise is usually described by Equation 3, with the additional requirement that the phases ϕ_1, ϕ_2, ϕ_3, ... be random (uniformly distributed between 0 and 2π). Under this assumption, it has been shown (Boschi & Weemstra, 2015; Weemstra et al., 2014) that, if the statistical expectation (e.g., Bendat & Piersol, 2011, Equation 3.8) $E[...]$ of Equation 4 is taken, the $j \neq k$ terms ("cross terms") cancel out and

$$E\left[s(\mathbf{x}_A,\omega)s^*(\mathbf{x}_B,\omega)\right] = h^2(\omega)\sum_{j=1}^{N_S} G^d_{2D}(\mathbf{x}_A,\mathbf{x}_j,\omega)G^{d*}_{2D}(\mathbf{x}_B,\mathbf{x}_j,\omega). \tag{5}$$

In the following, we shall drop the symbol $E[...]$ for the sake of simplicity. In a passive seismology experiment as the ones we are concerned with, statistical expectation cannot be evaluated directly from the data, which are seismic traces of finite duration. It is assumed that the finite-time cross correlation of seismic ambient noise coincides with its expectation. Our work hypothesis, similar, e.g., to Boschi and Weemstra (2015), is that this condition is approximately verified, in ambient-noise seismology, if sufficiently long time series (typically one year) are considered: in that case, a large number of sources distributed over the entire real plane, with random uncorrelated phases, should eventually be sampled. In practice, we call "diffuse" (e.g., Boschi & Weemstra, 2015, Section 3; Kinsler et al., 1999, Section 12.1) a wave field that meets this requirement. (The purpose of this study, in a sense, is to evaluate how far real data are from such an idealized situation).

As shown by Boschi et al. (2019), under this assumption the sum at the right-hand side (RHS) of Equation 4 can be replaced by an integral, and combined with the reciprocity theorem for a lossy membrane (Section 2.2 of Boschi et al., 2019) to yield

$$s(\mathbf{x}_A,\omega)s^*(\mathbf{x}_B,\omega) \approx -\frac{h^2(\omega)\rho}{2\sqrt{2\pi}\alpha\omega c}\Im\left[G^d_{2D}(\mathbf{x}_A,\mathbf{x}_B,\omega)\right], \tag{6}$$

where the operator $\Im[\ldots]$ maps a complex number into its imaginary part, ρ is the surface density of noise sources, and the factor $1/\sqrt{2\pi}$ arises from the correction of the algebraic error found in Boschi et al. (2019, 2020). Equation 6 stipulates that the amplitude of the cross correlation of ambient-noise recordings carries the information on the surface-wave attenuation coefficient α. This means that α can be retrieved from the data, if interstation phase velocity and spatial density and power spectral density of noise sources are known.

2.3. Power Spectral Density as Normalization Term

As shown by Boschi et al. (2019), the RHS of Equation 6 can be manipulated algebraically, to find an expression for the cross correlation of ambient noise where the source parameters $h^2(\omega)$ and ρ conveniently cancel out. In the following, we rederive the result of Boschi et al. (2019) in a slightly different fashion, showing explicitly that our formulation is in agreement with that of Nakahara (2012). (The result of Nakahara (2012) had been overlooked by Boschi et al. (2019).

Let us rewrite Equation 2 as

$$G^d_{2D}(x_1,x_2,\omega) \approx -\frac{i}{4\sqrt{2\pi}c^2}\left[J_0\left(\frac{\omega|\mathbf{x}_A-\mathbf{x}_B|}{c}\right)-iY_0\left(\frac{\omega|\mathbf{x}_A-\mathbf{x}_B|}{c}\right)\right]e^{-\alpha|\mathbf{x}_A-\mathbf{x}_B|} \tag{7}$$

(e.g., Boschi & Weemstra, 2015), where J_0 and Y_0 denote zeroth-order Bessel functions of the first and the second kind (e.g., Abramowitz & Stegun, 1964), respectively. Substituting Equation 7 into 6 yields

$$s(\mathbf{x}_A,\omega)s^*(\mathbf{x}_B,\omega) \approx -\frac{h^2(\omega)\rho}{16\pi\alpha\omega c^3}J_0\left(\frac{\omega|\mathbf{x}_A-\mathbf{x}_B|}{c}\right)e^{-\alpha|\mathbf{x}_A-\mathbf{x}_B|}. \tag{8}$$

It follows from Equation 8 that cross correlating the signal recorded at an arbitrary location $\mathbf{x}$ with itself, one obtains

$$|s(\mathbf{x},\omega)|^2 \approx \frac{h^2(\omega)\rho}{16\pi\alpha\omega c^3}. \tag{9}$$

Similar to Boschi et al. (2019), this formulation provides an analytical expression for $h^2(\omega)$ via Equation 9, which can be rewritten

$$\begin{aligned} h^2(\omega) &\approx \frac{16\pi\alpha\omega c^3}{\rho}|s(\mathbf{x},\omega)|^2 \\ &\approx \frac{16\pi\alpha\omega c^3}{\rho}<|s(\mathbf{x},\omega)|^2>_{\mathbf{x}}, \end{aligned} \tag{10}$$

where following the assumption that h is the same for all noise sources, we replaced $|s(\mathbf{x},\omega)|^2$ with its average $<|s(\mathbf{x},\omega)|^2>_{\mathbf{x}}$ over all available receiver locations $\mathbf{x}$. Upon dividing Equation 8 by 9, we find

$$\frac{s(\mathbf{x}_A,\omega)s^*(\mathbf{x}_B,\omega)}{<|s(\mathbf{x},\omega)|^2>_{\mathbf{x}}} \approx J_0\left(\frac{\omega|\mathbf{x}_A-\mathbf{x}_B|}{c}\right)e^{-\alpha|\mathbf{x}_A-\mathbf{x}_B|}, \tag{11}$$

where again, $|s(\mathbf{x},\omega)|^2$ is replaced by the average $<|s(\mathbf{x},\omega)|^2>_{\mathbf{x}}$. Importantly, Equation 11, adopted in this study, coincides with Equation 52 of Aki (1957), except for the damping term $e^{-\alpha|\mathbf{x}_A-\mathbf{x}_B|}$, and is consistent with Equation 9 of Prieto et al. (2009) and Equation 31 of Nakahara (2012).

Equation 11 should be compared with Equation 30 of Boschi et al. (2019), i.e.,

$$\frac{s(\mathbf{x}_A,\omega)s^*(\mathbf{x}_B,\omega)}{<|s(\mathbf{x},\omega)|^2>_{\mathbf{x}}} \approx \frac{c}{\omega\pi I(\alpha,\omega,c)}J_0\left(\frac{\omega|\mathbf{x}_A-\mathbf{x}_B|}{c}\right)\frac{e^{-\alpha|\mathbf{x}_A-\mathbf{x}_B|}}{\alpha}, \tag{12}$$

where the mentioned algebraic error (a factor $1/\sqrt{2\pi}$) has been corrected and

$$I(\alpha,\omega,c) = \int_0^\infty dr\, r\left|H_0^{(2)}\left(\frac{\omega r}{c}\right)\right|^2 e^{-2\alpha r}. \tag{13}$$

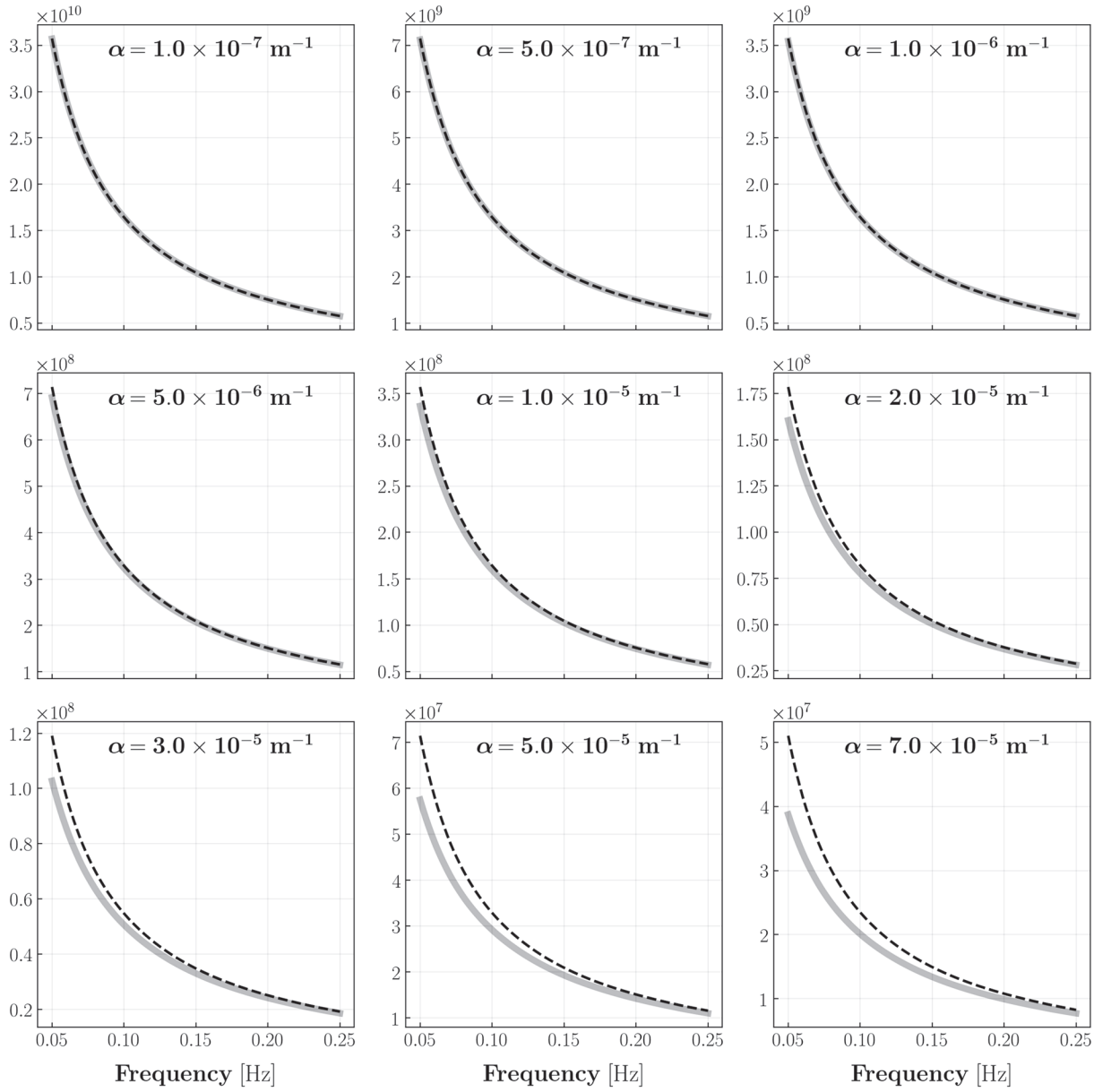

Figure 1. $I(\alpha, \omega, c)$ (gray, solid) and its analytical counterpart $\frac{c}{\pi\alpha\omega}$ (black, dashed) as functions of frequency, shown for different values of attenuation coefficient α. The phase velocity $c = c(\omega)$ is chosen to vary smoothly between 0.05 Hz (where $c = 3526$ ms^{-1}) and 0.25 Hz (2851 ms^{-1}), as illustrated in Figure S1. The same values of $c(\omega)$ are employed in the numerical simulations of Section 4.

Comparing Equations 12 and 11 provides an analytical expression for the integral at the right-hand side of Equation 13,

$$I(\alpha,\omega,c) \approx \frac{c}{\pi\alpha\omega}, \tag{14}$$

which Boschi et al. (2019) were unable to solve analytically. We show in Figure 1 that our numerical evaluation of $I(\alpha, \omega, c)$ (which exploits Gaussian quadrature, as provided by the SciPy Python library, Jones et al., 2001) is consistent with the expression at the right-hand side of Equation 14, if the conditions for the theoretical validity of our formulation are met. This further validates the formulation of Boschi et al. (2019).

The left-hand side (LHS) of both (11) and (12) represents the data, i.e., the normalized cross correlation of ambient noise records, while its RHS is our theoretical model. Importantly, as first pointed out by Boschi et al. (2019), $h(\omega)$ and ρ cancel out in the derivation that leads to Equation 11 and/or 12; it follows that these equations can be used, through an inverse problem, to determine α from the data without prior knowledge of source density and frequency content (as long as both are constant in space). In addition, if the LHS of Equations 11 and 12 is calculated as an ensemble-average of relatively small temporal windows with respect to the entire recording time, the normalization term $<|s(\mathbf{x},\omega)|^2>_{\mathbf{x}}$ mitigates the effect of possible anomalous, ballistic signals like, e.g., large or nearby earthquakes (Boschi et al., 2019). This is often necessary when working with real data and commonly accomplished by one-bit normalization or spectral whitening (e.g., Bensen et al., 2007); these empirical normalization terms, however, albeit useful for retrieving phase or group velocities since they leave the phase of the cross correlations unchanged, are doomed to introduce a bias in their amplitude and therefore in the resulting estimates of α (Weemstra et al., 2014).

We emphasize that Equation 11 (or 12) only holds if all our theoretical assumptions on the nature of ambient noise and propagation medium are valid, i.e., (i) the seismic ambient field is diffuse, (ii) source density and frequency content are both constant in space, and (iii) $\alpha \ll \omega/c$; in such scenario, both its RHS and LHS are purely real. When working with observational data, these assumptions are not strictly verified, and the numerical value of the LHS, as obtained from the data, is only approximately equal to the theoretical model at the RHS; this is why in ambient-noise literature empirical Green's functions commonly show a nonzero imaginary part, and are referred to as "complex coherency" (e.g., Weemstra et al., 2014) to distinguish them from the true Green's function.

3. Inverse Problem

Equation 11 allows to formulate an inverse problem to determine α from cross correlations of recorded ambient signal. Because Equation 11 holds for all station pairs, it is desirable that the cost function be related to the weighted sum of the squared differences between LHS and RHS of Equation 11, calculated for each station pair; since the RHS is an oscillatory function of ω (through the Bessel function J_0), and α only affects its envelope but not its oscillations (e.g., Boschi et al., 2019; Prieto et al., 2009), we introduce the envelope function env to define the cost function

$$C(\alpha,\omega) = \sum_{i,j} \left|\mathbf{x}_i - \mathbf{x}_j\right|^2 \left| \mathrm{env}\left[\frac{s(\mathbf{x}_i,\omega)\, s^*(\mathbf{x}_j,\omega)}{<|s(\mathbf{x},\omega)|^2>_{\mathbf{x}}} \right] - \mathrm{env}\left[J_0\left(\frac{\omega\,|\mathbf{x}_i - \mathbf{x}_j|}{c_{ij}(\omega)} \right) e^{-\alpha|\mathbf{x}_i - \mathbf{x}_j|} \right] \right|^2, \tag{15}$$

where $\mathbf{x}_i$ and $\mathbf{x}_j$ denote the positions of the two receivers, and the sum spans all possible station pairs. The weight $\left|\mathbf{x}_i - \mathbf{x}_j\right|^2$ is chosen based on the fact that larger interstation distances are associated with smaller amplitudes of the cross correlations, due to geometrical spreading, which would result in smaller absolute values of misfit if not weighted accordingly. $c_{ij}(\omega)$ denotes the average phase velocity, at frequency ω, between receivers at $\mathbf{x}_i$ and $\mathbf{x}_j$; for each station pair, we determine its value before minimizing $C(\alpha, \omega)$ by application of the method described by Kästle et al. (2016). The minimum of $C(\alpha, \omega)$ can then be found through some form of "grid-search" over α, for a discrete set of values of ω. Formula 15 for $C(\alpha, \omega)$ was selected after experimenting several other options, as partly documented in Boschi et al. (2019). After a suite of preliminary tests, we chose to implement the envelope function by fitting a combination of cubic splines (De Boor, 1978) to the maxima of the absolute value of the real part of their arguments; the envelopes are then smoothed by means of a running average performed with a Savitzky-Golay filter (Savitzky & Golay, 1964). Smoothing is motivated by the fact that, if the anelastic properties of the Earth are assumed to be smoothly varying with depth, the same behavior is expected for the amplitude of adjacent peaks of the real coherency; abrupt amplitude variations are ascribed to a nonperfectly diffuse wavefield or, in the case of real recordings, simply to noisiness of the empirical Green's function.

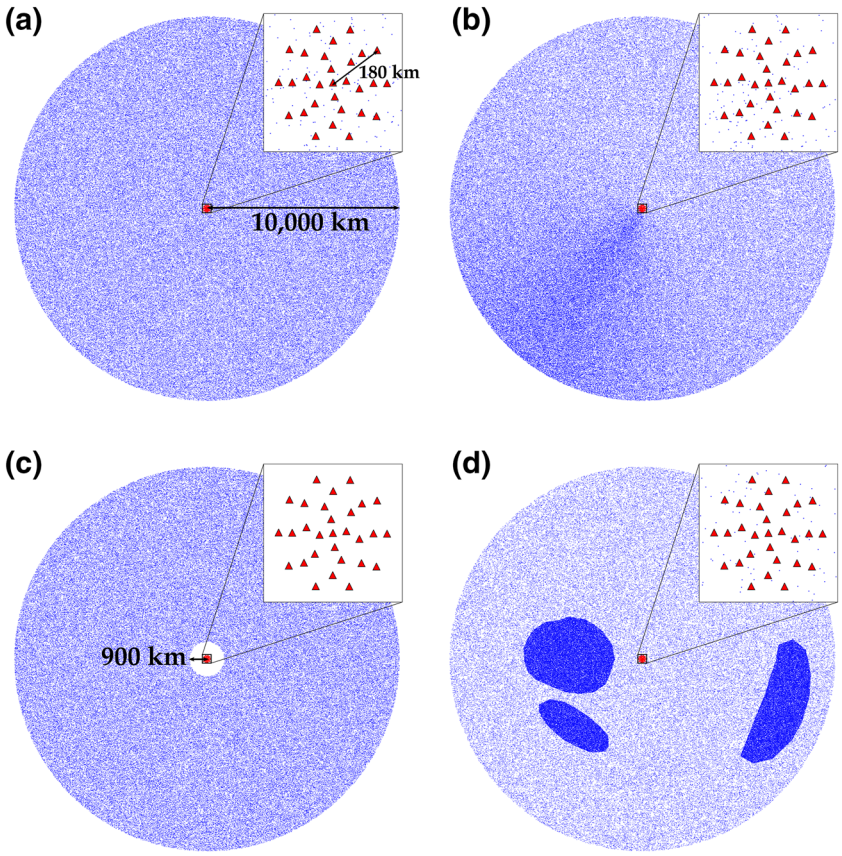

Figure 2. Sources (blue dots) and stations (red triangles) used for simulating seismic noise. (a), (b), (c), and (d) indicate the source distributions used in Sections 4.1 (uniform source distribution), Section 4.2 (azimuth-dependent source density), Section 4.3 (no sources in the near field), and Section 4.4 ("patchy" source distribution), respectively.

The summation over receiver pairs i, j at the RHS of 15 involves all the available receivers and, if the array has good azimuthal coverage, most azimuths of wave propagation. Minimizing $C(\alpha, \omega)$ therefore involves finding one function $\alpha(\omega)$ such that a good fit is simultaneously achieved at all azimuths; this has a regularizing effect on the inversion, and should reduce the effects of nonhomogeneity in azimuthal source distribution.

Previous studies (e.g., Prieto et al., 2009; Weemstra et al., 2013) formulated inverse problems whose data consisted of azimuthally averaged cross correlations calculated over several station pairs; this was based on the idea that azimuthal averaging is necessary to retrieve a reliable, purely real empirical Green's function (e.g., Asten, 2006; Yokoi & Margaryan, 2008). Menon et al. (2014), however, show that slightly different interstation distances or a laterally inhomogeneous phase velocity would introduce a phase offset of the cross correlations involved in the average. This would result in an "attenuation-like" effect (Figure 2 of Menon et al., 2014), i.e., in a fictitious decrease of the amplitude of the averaged coherency and thus in a bias of the estimates of α.

4. Numerical Validation

We simulate ambient signal via a very large number of randomly distributed, uncorrelated point sources. We next solve an inverse problem, as described above, to retrieve the theoretical value of α; we also verify numerically the emergence of coherent signal in the cross correlations due to cancellation of cross terms in Equation 4, and the validity of Equation 10, which relates recorded ambient noise and the frequency spectrum of ambient-noise sources. The simulation is carried out in four different experimental setups. First, we present the "ideal" case of a spatially uniform distribution of sources (Figure 2a). Since real-world ambient

sources are not distributed uniformly (e.g., Hillers et al., 2012), we next discuss the cases of an azimuthally heterogeneous source distribution (Figure 2b) and of a distribution characterized by absence of noise sources in the vicinity of the receivers (Figure 2c). Finally, we show the results obtained through a "patchy" distribution, characterized by a variable density of sources both in space and in azimuth (Figure 2d).

4.1. Uniform Source Distribution

Our first experimental setup consists of 200,000 point sources randomly distributed both in the near and far field of 29 receivers, within a circle of radius $R = 1 \times 10^7$ m centered at the receiver array (Figure 2a). Source locations are defined by their polar coordinates θ, r with respect to one station located at the center of the array; random values of θ between 0 and 2π, and of n between 0 and 1 are generated, and $r = R\sqrt{n}$ (the square root results in a linear growth of the number of sources with increasing distance from the center of the circle, hence constant source density in space). The receivers are randomly deployed in the central part of such distribution on 4 concentric circles, with radii of 45, 90, 135, and 180×10^3 m.

4.1.1. Simulation of Seismic Ambient Noise

In each of two experiments, synthetic data are generated using different models of attenuation, i.e., (i) constant attenuation with $\alpha = 1 \times 10^{-6}$ m^{-1}, and (ii) frequency-dependent $\alpha = \alpha(\omega)$, chosen to vary linearly from 3×10^{-7} at 0.05 Hz to 1×10^{-6} m^{-1} at 0.25 Hz. (A third experiment, with constant $\alpha = 5 \times 10^{-7}$ m^{-1} is illustrated in the supplementary materials.) In all numerical simulations, we employed a fixed, frequency-dependent phase velocity $c = c(\omega)$, which decreases monotonously (and almost linearly) between 0.05 Hz (where $c = 3526$ ms^{-1}) and 0.25 Hz (2851 ms^{-1}), with a slight kink around 0.07 Hz where its derivative with respect to time decreases with increasing frequency (Figure S1). We consider these values to be realistic, based, e.g., on Mitchell (1995) and Ekström (2014).

Each numerical test consisted of 25,000 *realizations* (Cupillard & Capdeville, 2010; Weemstra et al., 2015). At each realization, every source emits an independent signal of constant amplitude $h(\omega) = 1$ and random phase ϕ between 0 and 2π. The displacement at the receivers due to the impulsive sources is computed, at each realization, via Equation 3; the LHS of Equation 11 is then implemented for a pair of stations $\mathbf{x}_A$, $\mathbf{x}_B$ by ensemble-averaging the normalized cross correlations (calculated for each realization k) over N_R realizations,

$$\frac{s(\mathbf{x}_A,\omega)s^*(\mathbf{x}_B,\omega)}{<|s(\mathbf{x},\omega)|^2>_{\mathbf{x}}} = \frac{1}{N_R}\sum_{k=1}^{N_R}\frac{s_k(\mathbf{x}_A,\omega)s_k^*(\mathbf{x}_B,\omega)}{<|s(\mathbf{x},\omega)|^2>_{\mathbf{x}}}. \tag{16}$$

4.1.2. Cancellation of Cross Terms and Source Spectrum

Real and imaginary parts of normalized cross correlations, calculated by ensemble-averaging over an increasing number of realizations as in the RHS of Equation 16, are shown in Figure 3 for a pair of receivers with interstation distance of 67,600 m. For both chosen values of α, the increase in the smoothness of the real parts and the decrease in the amplitude of the imaginary parts with the number of realizations bring evidence of the cancellation of cross terms of Equation 4. An analogous result is obtained through the synthetic recordings generated with $\alpha = 5 \times 10^{-7}$ m^{-1}, as illustrated in Figure S2.

Equation 10 indicates that it is possible to retrieve the source spectrum $h(\omega)$ if source density ρ and attenuation coefficient are known, provided that h is the same for all sources (Section 2.2); we show in Figure 4 that, implementing Equation 10, $h(\omega) = 1$ is retrieved correctly, at least to the second decimal digit, in case of a uniform source distribution. This result validates numerically the derivation of Equation 10. Figure 4 also shows that, when the true α is unknown, the observed values of α (obtained by minimization of the cost function $C(\alpha, \omega)$, as explained in the following paragraph) can be used to implement Equation 10, allowing one to achieve only slightly worse accuracy.

4.1.3. Retrieval of the Attenuation Coefficient

The cost function $C(\alpha, \omega)$ in Equation 15 is evaluated by means of a 1-D grid search over 275 values of α evenly spaced on logarithmic scale between 5×10^{-8} and 1×10^{-4} m^{-1}. Figure 5 shows that, on average, the

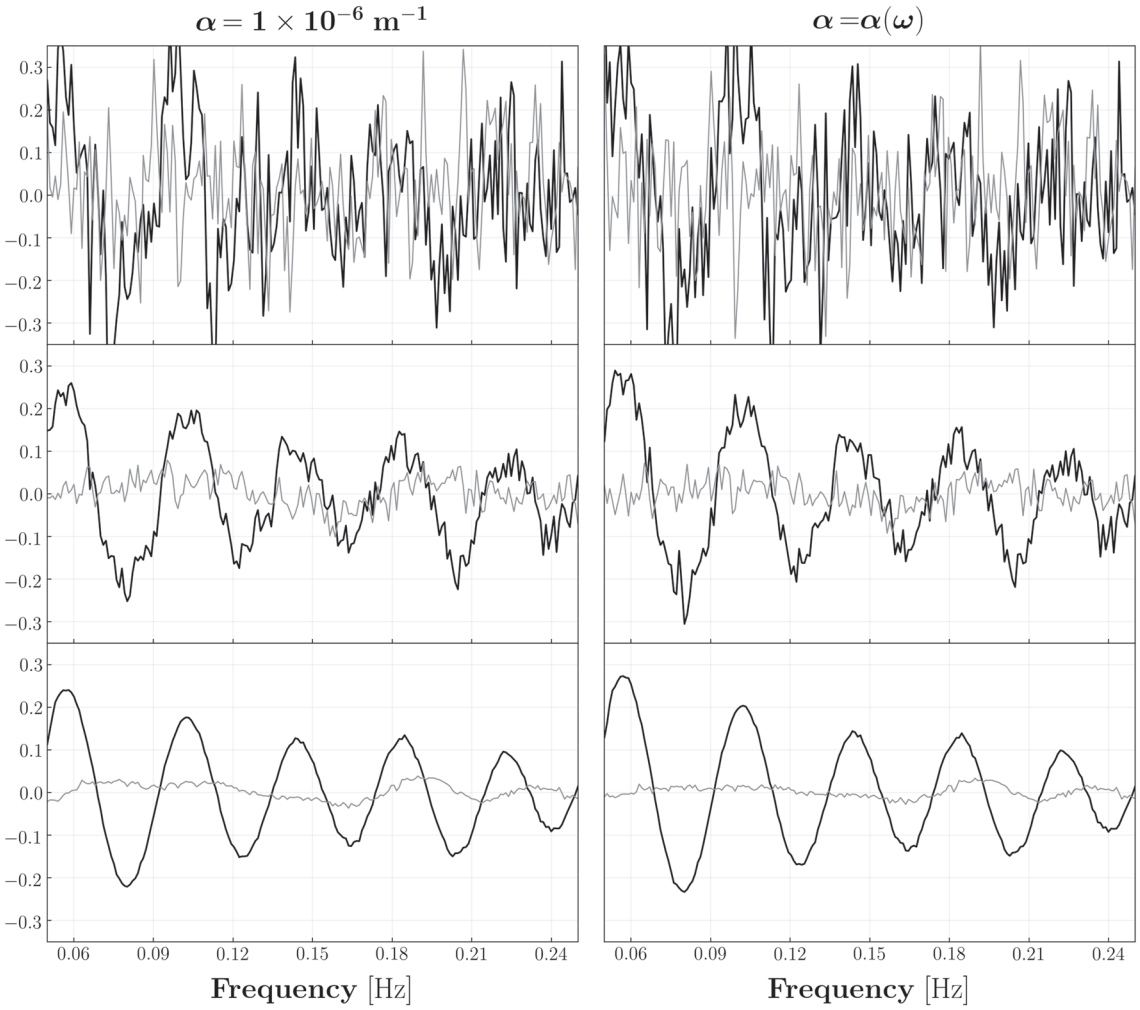

Figure 3. Real (black) and imaginary (gray) parts of LHS of Equation 16, obtained for a pair of receivers with interstation distance of 67,600 m by ensemble-averaging over (top) 25, (middle) 500, and (bottom) 25,000 realizations. Results are shown for both $\alpha = 1 \times 10^{-6}$ and $\alpha = \alpha(\omega)$, used in the experimental setup of Section 4.1 (uniform source distribution). Note the slightly different amplitudes of the real coherencies, as expected for media characterized by different attenuation coefficients.

minima of $C(\alpha, \omega)$ correspond to the values of α used for generating synthetic recordings, i.e., the synthetic test is successful. In the same figure, we show for both numerical tests the datafit obtained by substituting into Equation 11 the values of $\alpha(\omega)$ retrieved by minimizing $C(\alpha, \omega)$, and can be considered good at all the investigated interstation distances. An analogous result is obtained through the synthetic recordings generated with $\alpha = 5 \times 10^{-7}$ m^{-1}, as illustrated in Figure S7.

4.2. Azimuth-Dependent Source Density

In a second numerical simulation, the spatial distribution of sources is modified while all other parameters are left unchanged; the nonuniformity in the source distribution is implemented by generating random values k between 0 and 2π, and obtaining source azimuth from k via the formula $\theta = k + \frac{1}{2}\cos\left(k - \frac{4}{5}\pi\right)$; $r = R\sqrt{n}$, with $0 \le n < 1$, as above. The spatial distribution of sources thus obtained is characterized by a higher density to the South-West of the array (Figure 2b). Synthetic data are generated using the phase velocity $c = c(\omega)$ of Section 4.1, and a constant attenuation coefficient $\alpha = 1 \times 10^{-6}$ m^{-1}. In analogy with the first numerical test, seismic ambient noise has been simulated for 25,000 realizations, with $h(\omega) = 1$ and random phase ϕ between 0 and 2π.

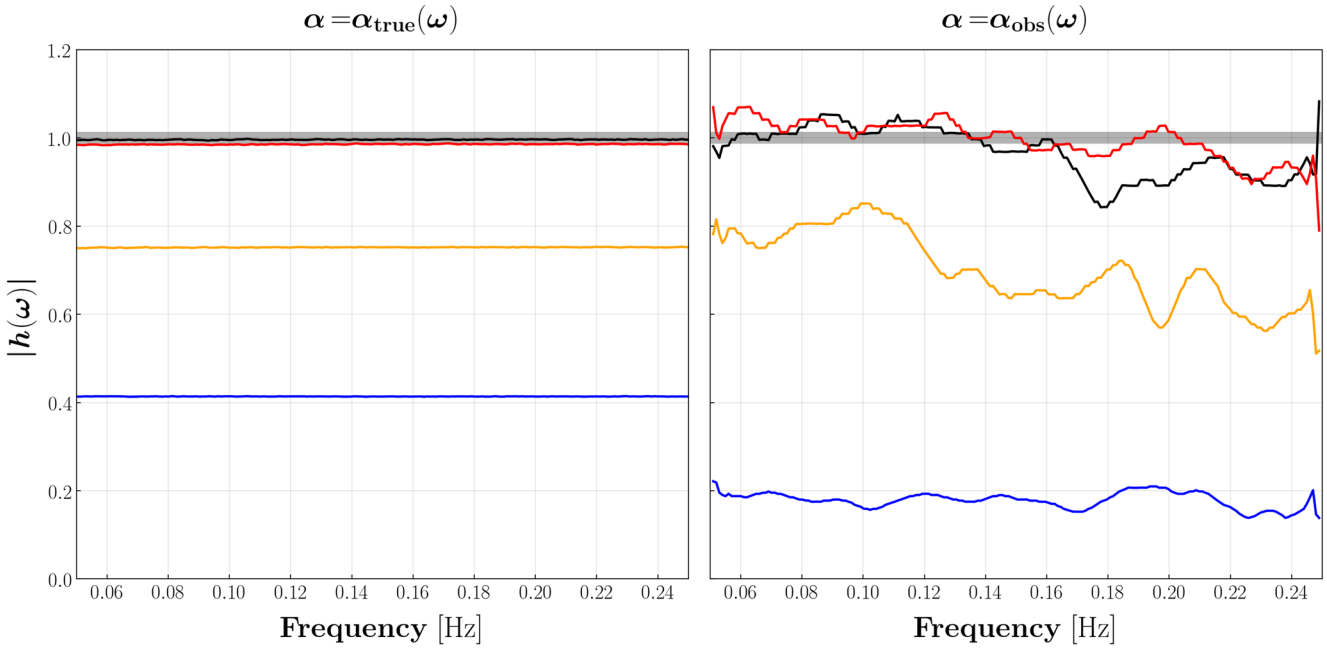

Figure 4. Absolute value of source amplitude $|h(\omega)|$, retrieved in the synthetic tests described in Sections 4.1 (uniform source distribution, black), 4.2 (azimuth-dependent source density, red), 4.3 (absence of near-field sources, blue), and 4.4 ("patchy" source distribution, orange). In all cases, synthetic data are computed with $h(\omega) = 1$ (gray) and $\alpha = 1 \times 10^{-6}$ m^{-1}. $|h(\omega)|$ is calculated by substituting into Equation 9 both the true value of α (left) and the ones inferred from the cross correlations (right), and then taking the square root; the estimates of α have been obtained by minimizing the cost function $C(\alpha, \omega)$ (Section 3). In the case of a uniform source distribution, analogous results are obtained through the synthetics generated with $\alpha = 5 \times 10^{-7}$ m^{-1} and $\alpha = \alpha(\omega)$, as shown in Figure S5.

We verified the emergence of coherent signal in the normalized cross correlations at increasing number of realizations, as illustrated in Figure S3. As expected, the cross terms cancel out, but, in comparison with the previous section, we found slightly larger imaginary parts of the cross spectra; this can be ascribed to the nonuniform distribution of the noise sources (see Section 2). The source spectrum $h(\omega)$, retrieved from the synthetics, is shown in Figure 4 to be closed to the true value of 1; this indicates that Equation 10 allows estimating the frequency content of the noise sources accurately, even if the assumption of diffuse ambient field is not exactly met.

Following the same procedure as in Section 4.1.3, we obtained minima of $C(\alpha, \omega)$ which correspond, on average, to the true attenuation $\alpha = 1 \times 10^{-6}$ m^{-1}. This is illustrated in Figure 6, together with the datafit obtained by substituting into Equation 11 the best values of $\alpha(\omega)$ for the same station pairs employed in Figure 5.

The above results show that, even if the spatial distribution of noise sources is slightly nonuniform, the value of $\alpha(\omega)$ can be reconstructed correctly from the cross correlation of ambient noise: we have achieved this, as anticipated, by neglecting possible lateral heterogeneities in $\alpha(\omega)$, and minimizing a cost function where as many azimuths of propagation as possible are simultaneously included. In practice, this means that surface-wave attenuation can be estimated based on ambient noise, even when the noise field is not exactly diffuse. This is indeed the case in most practical applications.

4.3. No Near-Field sources

Sources are uniformly distributed in space, as in Section 4.1, but starting at a minimum distance of 900×10^3 m from the station that defines the center of the array (Figure 2c). We implement 25,000 realizations with the same phase velocity $c = c(\omega)$ as before, attenuation $\alpha = 1 \times 10^{-6}$ m^{-1}, and $h(\omega) = 1$. Again, a random phase ϕ between 0 and 2π, newly generated at each realization, is assigned to each source.

In analogy with the experiments above, we verified the emergence of coherent signal in the cross correlations due to the cancellation of cross terms. The amplitude of the imaginary part of the cross spectra turned out to be similar to that obtained for an azimuthally heterogeneous source distribution (see Figure S4). On

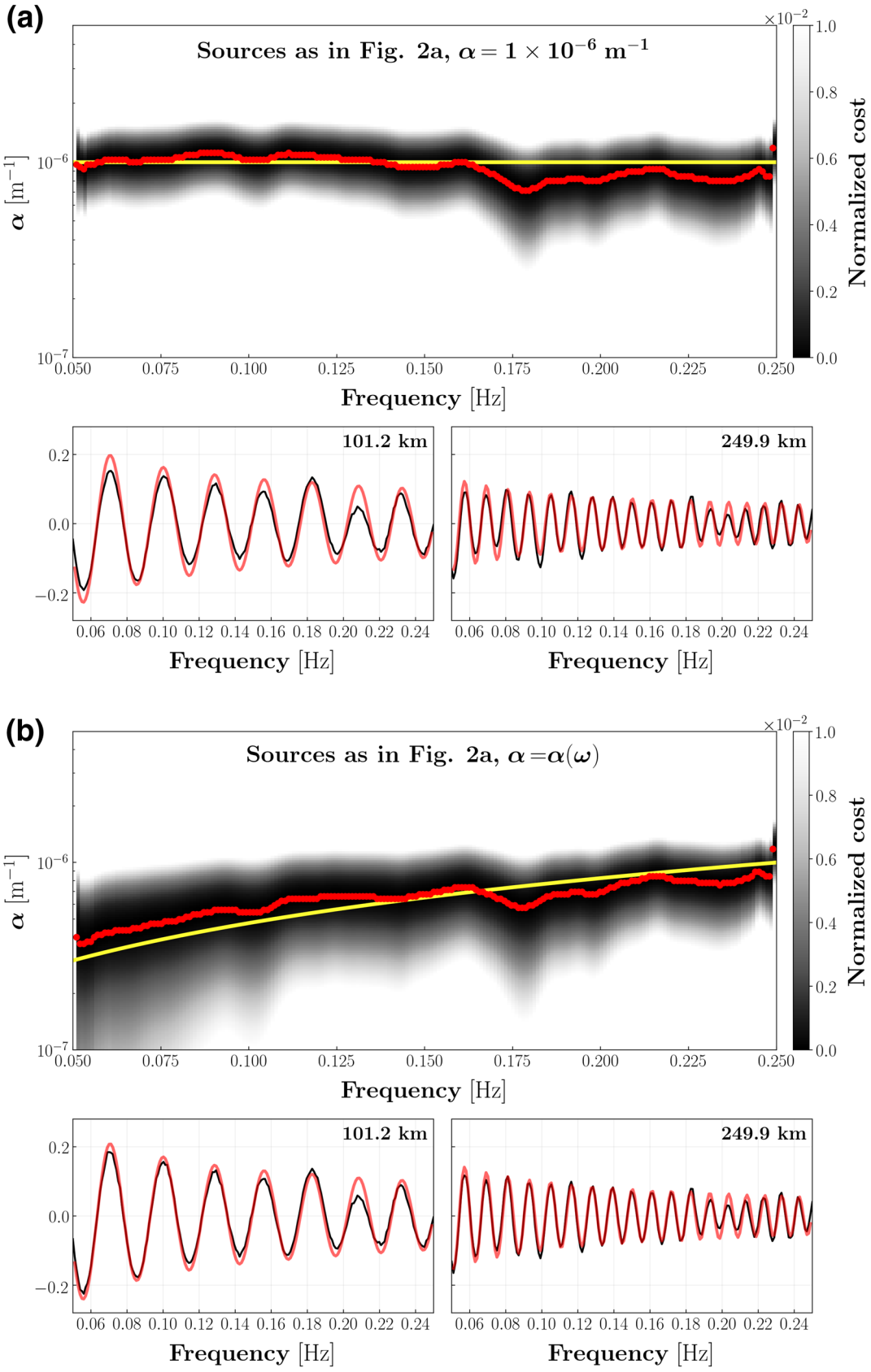
(a)
Sources as in Fig. 2a, $\alpha = 1 \times 10^{-6}$ m^{-1}
α [m^{-1}]
Frequency [Hz]
Normalized cost
101.2 km
249.9 km
(b)
Sources as in Fig. 2a, $\alpha = \alpha(\omega)$
α [m^{-1}]
Frequency [Hz]
Normalized cost
101.2 km
249.9 km

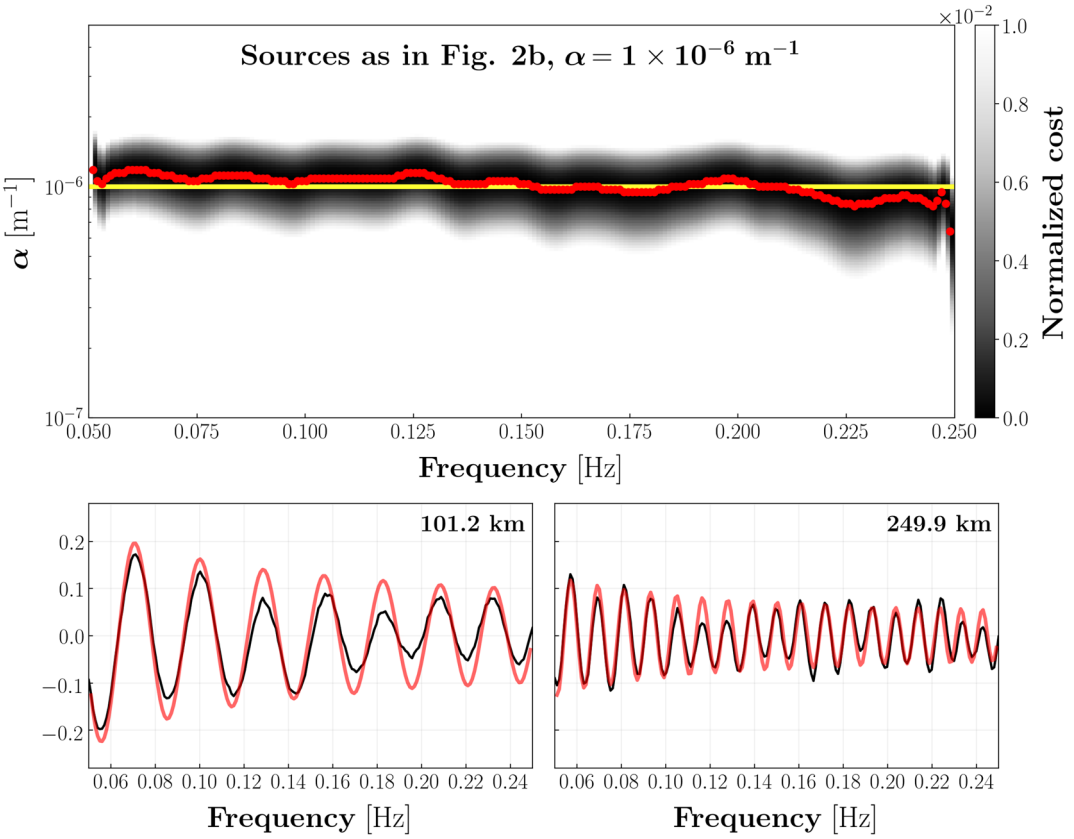

Figure 6. Top panel: cost function $C(\alpha, \omega)$ associated with the numerical experiment of Section 4.2 (azimuth-dependent source density) shown (after normalization) as a function of attenuation coefficient and frequency. Red dots mark the values of α for which $C(\alpha, \omega)$ is minimized at each frequency; the yellow line indicates the assumed attenuation model $\alpha = 1 \times 10^{-6}$ m^{-1}, used for generating synthetic recordings. Bottom: normalized cross correlations (black) fitted by the model (red) obtained by substituting into Equation 11 the values of $\alpha(\omega)$ which minimize $C(\alpha, \omega)$. Within each subplot, the interstation distance is indicated on the upper right.

the other hand, the real part is systematically larger than those observed in the previous experiments. As in Sections 4.1 and 4.2, we then used the synthetic data to quantify source spectrum $h(\omega)$ and attenuation $\alpha(\omega)$ (Figures 4 and 7). We infer from the results thus obtained that the absence of near-field sources leads to a significant underestimate of both $h(\omega)$ and $\alpha(\omega)$ (the latter by a factor of about 5), in agreement with the theoretical findings of Tsai (2011).

4.4. "Patchy" Source Distribution

About 100,000 sources are uniformly distributed in space, as in Section 4.1, and 100,000 sources are concentrated in discrete regions (Figure 2d). As in the previous section, we implemented 25,000 realizations using the phase velocity $c = c(\omega)$, attenuation $\alpha = 1 \times 10^{-6}$ m^{-1}, and $h(\omega) = 1$, attributing to each source a random phase ϕ between 0 and 2π newly generated at each realization.

We first used the so generated synthetic recordings to compute the normalized cross correlations, whose smoothness indicates that the cross terms canceled out, as predicted by the theory (Figure S5). Due to the

Figure 5. (a) Top panel: cost function $C(\alpha, \omega)$ associated with the numerical experiment of Section 4.1 (uniform source distribution) shown (after normalization) as a function of attenuation coefficient and frequency; red dots mark the values of α for which $C(\alpha, \omega)$ is minimized at each frequency; the yellow line indicates the assumed attenuation model $\alpha = 1 \times 10^{-6}$ m^{-1}, used for generating synthetic recordings. Bottom: normalized cross correlations (black) fitted by the model (red) obtained by substituting into Equation 11 the values of $\alpha(\omega)$ which minimize $C(\alpha, \omega)$. Within each subplot, the interstation distance is indicated on the upper right. (b) Same as (a), but obtained through the synthetic recordings generated with a frequency-dependent $\alpha = \alpha(\omega)$, varying between 3×10^{-7} m^{-1} at 0.05 Hz and 1×10^{-6} m^{-1} at 0.25 Hz.

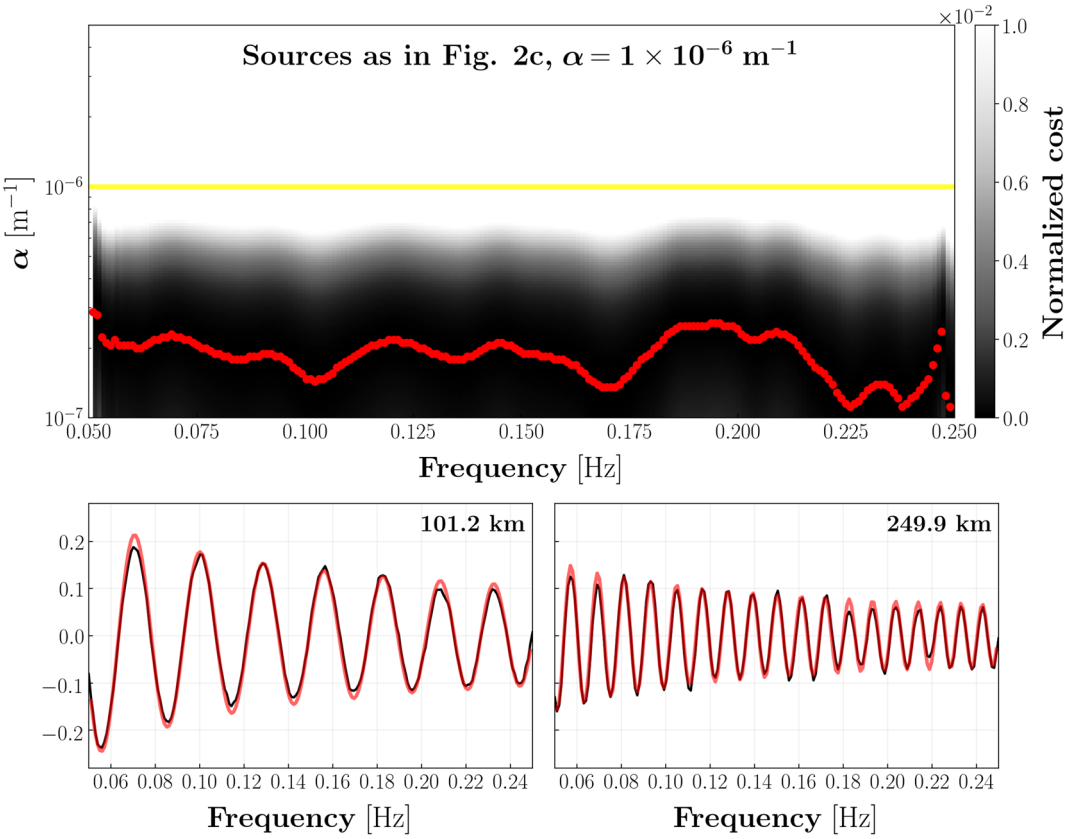

Figure 7. Same as Figure 6, but obtained through the numerical experiment of Section 4.3 (no sources in the near field).

strong lateral heterogeneity characterizing this source distribution, we found, on average, larger imaginary parts of the cross spectra than what we observed in the experiments above. We then used the cross spectra to reconstruct $h(\omega)$ (Figure 4), finding values ~25% less than the true frequency spectrum used to generate the synthetics: a much better result than what we achieved in the case of a distribution characterized by absence of near-field sources. Finally, we inverted the synthetic data using Equation 15 to obtain estimates of the attenuation coefficient that fluctuate around the true value of α. Overall, we observed a lower accuracy in this experimental setup than those of Sections 4.1 and 4.2 (compare Figure 8 with Figures 5 and 6), but still acceptable considering the extreme spatial and azimuthal heterogeneity of the source distribution.

5. Preliminary Application to a Small Subset of USArray

5.1. Data Set

We downloaded continuous vertical-component recordings from 33 broad-band receivers belonging to the transportable component of the USArray network (Figure 9) and operating between February 2007 and August 2008. Each seismogram has been demeaned, detrended, tapered (5%), and bandpass-filtered between 0.01 and 0.5 Hz before deconvolving the instrumental response to displacement; eventual gaps present in the waveforms have been zero-padded, in order to obtain continuous time-series. From all those continuous data, we computed 509 empirical Green's functions (i.e., LHS of Equation 11), by ensemble averaging cross spectra calculated in 6-h long windows. To reduce the effects of temporal variability and/or seasonality of noise sources, we only cross-correlated pairs of receivers that recorded simultaneously for more than 9 months.

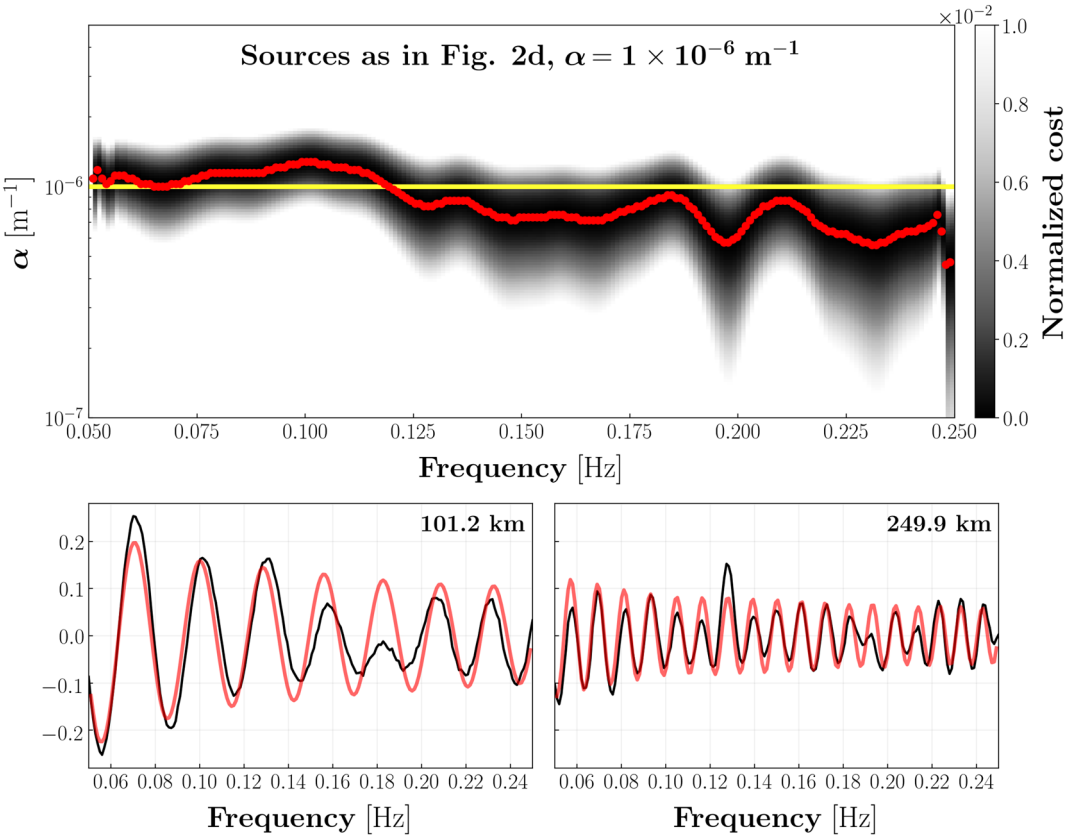

Figure 8. Same as Figures 6 and 7, but obtained through the numerical experiment of Section 4.4 ("patchy" source distribution).

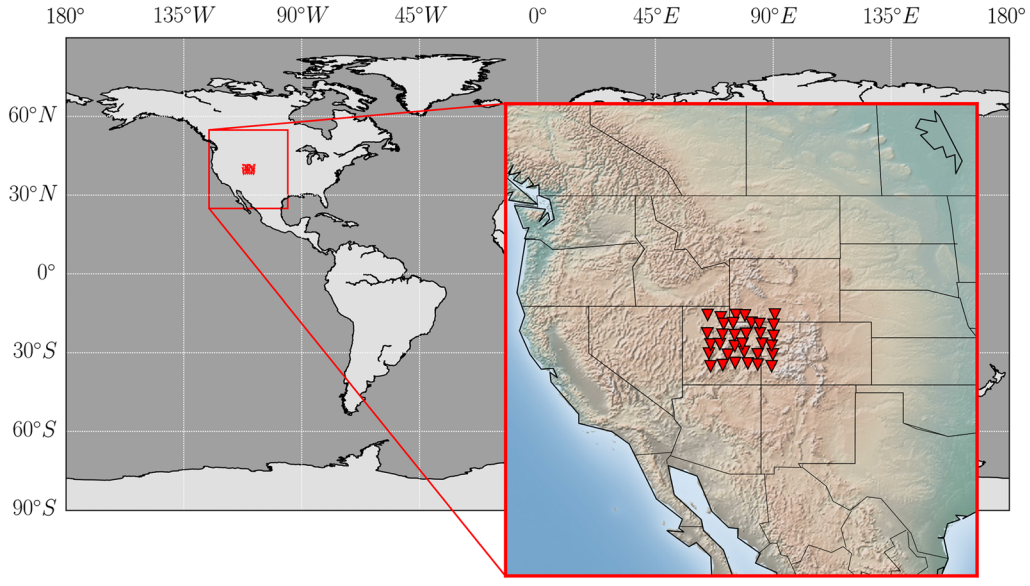

Figure 9. Seismic stations (red triangles) from the USArray project transportable network, forming the data set described in Section 5.1.

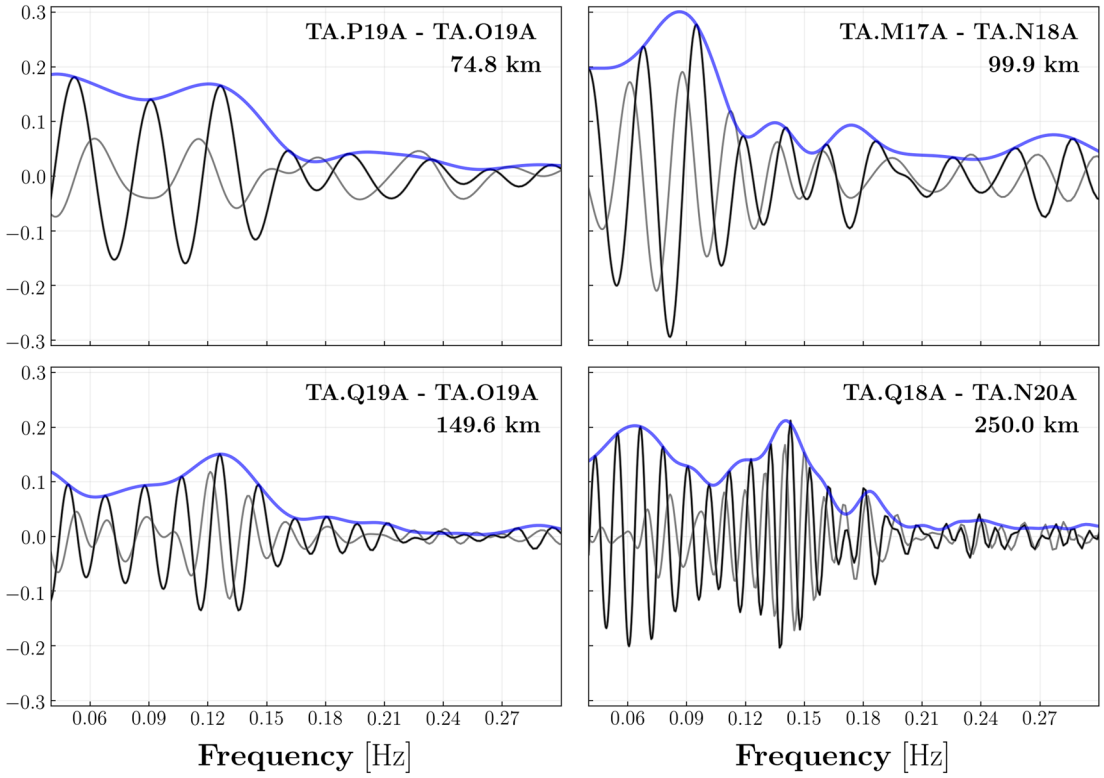

Figure 10. Real (black) and imaginary (gray) parts of smoothed (Section 5.1), normalized cross correlations calculated for four different station pairs. The envelope of the real parts, used in the inversion for α, is shown in blue. At the upper right corner of each subplot, station codes and interstation distance are specified.

We next "pre-process" the normalized cross correlation, to better isolate the fundamental-mode amplitude signal that is relevant to the subsequent attenuation inversion, i.e., the "stationary points" of the frequency-domain cross correlation curves (Figure 10). This processing was not carried out in the synthetic tests discussed above, but is likely to be necessary when dealing with real-world ambient signal. The procedure we have designed consists of three steps. (i) We inverse-Fourier transform our frequency-domain cross correlations to the time domain; (ii) we zero-pad the resulting time-domain traces at times corresponding to velocities lower than 2 km s^{-1} and higher than 5 km s^{-1} (the same cosine taper is applied at the two ends of this interval), i.e., all signal that is much faster or slower than the typical fundamental-mode surface wave; (iii) we forward-Fourier transform the padded cross correlations back to the frequency domain. Through this procedure, most of the signal that is not associated with the Rayleigh-wave fundamental mode (i.e., the Rayleigh-wave overtones; the body waves) is eliminated. By the properties of the Fourier transform, this has also the effect of "smoothing" the frequency-domain cross correlation (Figure 10).

The thus achieved (normalized) cross correlations served us to retrieve Rayleigh-wave dispersion curves in the frequency range between 0.3 and 0.04 Hz (we used the Kästle et al. (2016)'s automated algorithm) and the envelopes to be used in the inversion.

5.2. Signal-To-Noise Ratio

We show in Figure 10 four normalized cross correlations associated with receiver pairs that are characterized by significantly different interstation distances. The fact that the imaginary part of the empirical Green's function is nonzero indicates that the assumptions described in Section 2 are not exactly met by our observations, because the ambient wavefield is not perfectly diffuse (Boschi & Weemstra, 2015). To estimate possible azimuthal biases introduced in the recordings, we therefore performed a signal-to-noise ratio (SNR) analysis; this allows to assess the presence of preferential directionality of the noise sources,

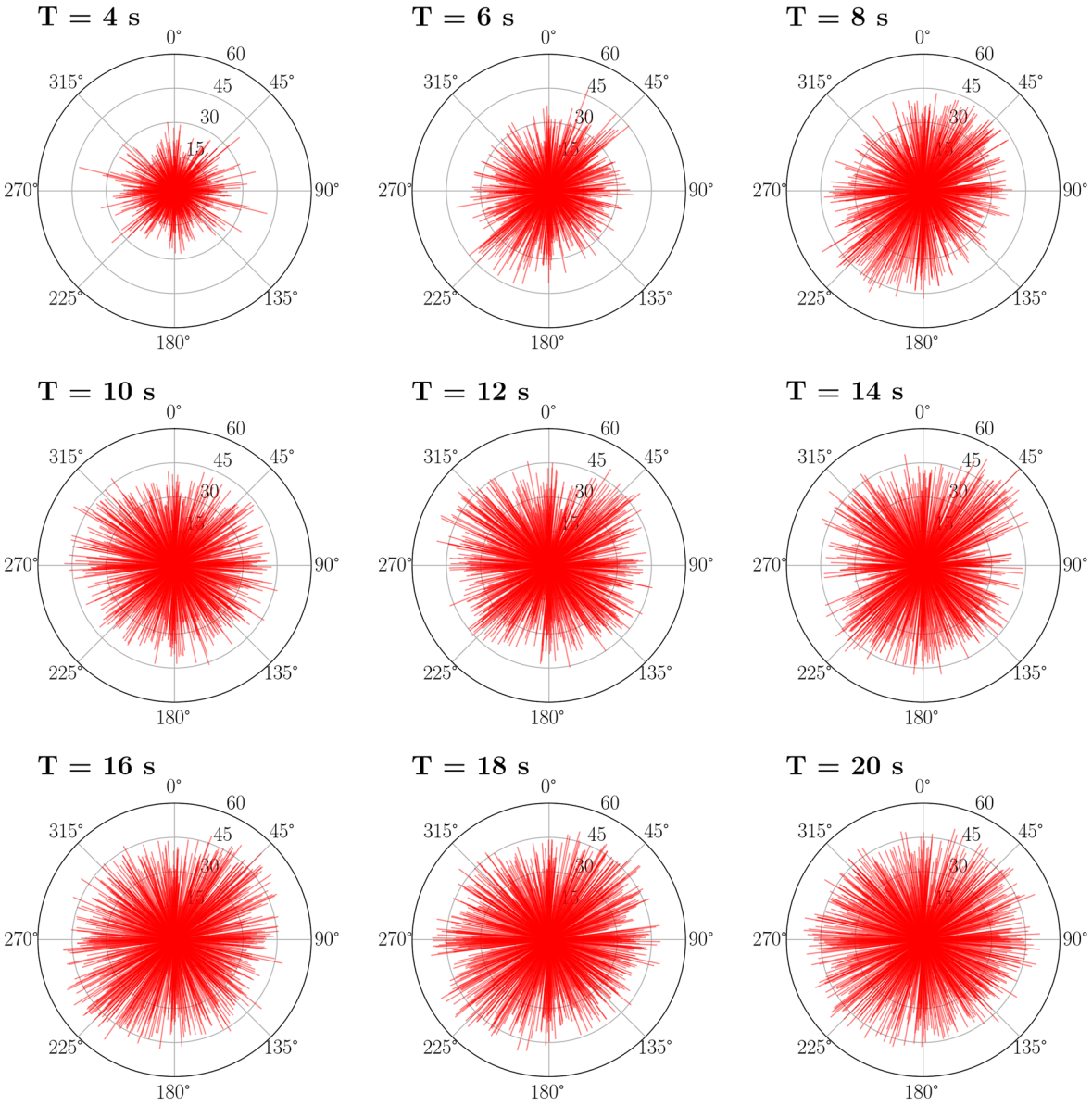

Figure 11. Signal-to-noise ratio at different periods as a function of azimuth, as inferred from the normalized cross correlations. The length of the red segments is determined by the value of SNR, while their orientation coincides with the azimuth/back-azimuth of the respective station pair. 0° corresponds to the north, 90° to the east, etc.

thus giving indication of the diffusivity of the ambient wavefield. The analysis has been carried out by narrow-bandpass filtering and inverse-Fourier transforming all the available cross spectra; in the time domain, the SNR is then calculated by taking the ratio of the maximum signal amplitude to the maximum of the trailing noise (e.g., Kästle et al., 2016; Yang & Ritzwoller, 2008). In this analysis, "signal" refers to the segment of ambient-noise cross correlation that contains the Rayleigh-wave fundamental mode propagating between the two relevant receivers. In practice, this corresponds to the temporal window identified by a velocity range between 2 and 4.2 km s^{-1}.

We infer from visual inspection of the results thus obtained (Figure 11) that the ambient field is relatively isotropic within the study area, at least in the frequency band associated with the *primary* microseisms, i.e., from ~10 s to ~20 s period, peaking at ~14 s (e.g., Friedrich et al., 1998): compare, e.g., with Figure 12 of Kästle et al. (2016), where a strong nonuniformity in the source distribution can be appreciated from

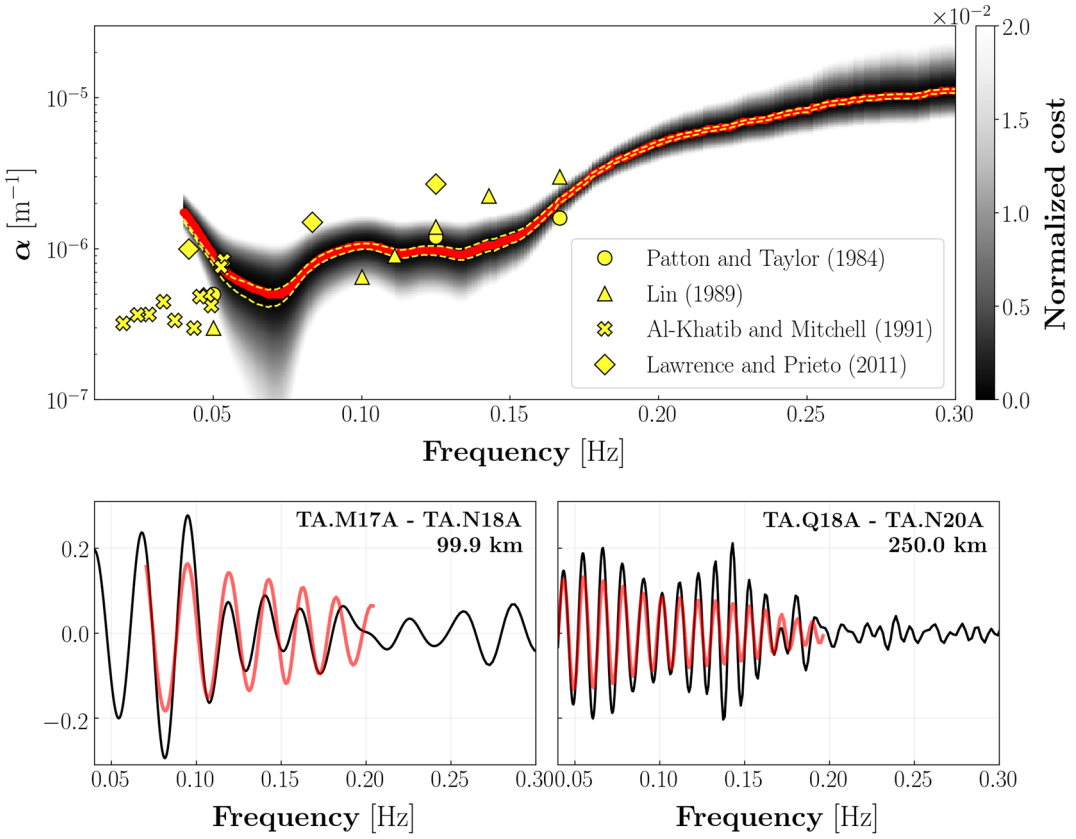

Figure 12. Top panel: cost function $C(\alpha, \omega)$ shown (after normalization) as a function of attenuation coefficient and frequency. The red dots mark the values of α for which $C(\alpha, \omega)$ is minimized at each frequency. The dashed yellow line is calculated, at each frequency, as $\mu \pm \sigma$, where μ and σ indicate mean and standard deviation of the values of α retrieved from the bootstrap analysis. Yellow marks indicate average measurements of alpha as collected in the vicinity of the study area in previous studies (i.e., ; Al-Khatib & Mitchell, 1991; Lawrence & Prieto, 2011; Lin, 1989; Patton & Taylor, 1984, as specified in the legend). Bottom: normalized cross correlations (black) fitted by the model (red) obtained by substituting into Equation 11 the values of $\alpha(\omega)$ which minimize the cost function $C(\alpha, \omega)$. The datafit is shown for the same station pairs of Figure 10. Within each subplot, station codes and interstation distance are indicated on the upper right. The frequency band spanned by the models is determined by the availability of phase-velocity measurements.

exactly the same analysis. Our measurements of SNR at the central periods of the *secondary* microseisms band are characterized by a relative maximum along the SW-NE direction (see the periods of 6 and 8 s in Figure 11). This was also noted by, e.g., Landès et al. (2010) and Tian and Ritzwoller (2015), who identified in the central Pacific Ocean a probable source region of secondary microseisms (see Figure 8 of Tian & Ritzwoller, 2015). However, the preferential directionality of noise emerging from our SNR analysis is less prominent. This result confirms the known seasonality of ambient noise sources (e.g., Hillers et al., 2012; Tanimoto et al., 2006). Ensemble-averaging over several months of recordings reduces this effect, and the resulting empirical Green's functions better approximate those that would be obtained from a truly diffuse ambient field.

5.3. Results and Discussion

To retrieve the attenuation coefficient within the study area, we performed a 1-D grid search over 275 values of α evenly spaced on a logarithmic scale between 5×10^{-8} and 1×10^{-4} m^{-1}; in analogy with Section 4, minimization of the cost function $C(\alpha, \omega)$ allowed us to identify the best fitting value of α at each frequency, as shown in Figure 12 . In the same Figure we also show, for four different station pairs, the datafit obtained by substituting into Equation 11 the values of $\alpha(\omega)$ which minimize $C(\alpha, \omega)$. The source spectrum of the

study area, as inferred from our measurements of $\alpha(\omega)$, $c(\omega)$, average power spectral density, and assuming a constant source density ρ, is shown in the supplementary materials (Figure S8).

We assessed the uncertainty associated with α via a bootstrap analysis: in practice, we minimized $C(\alpha, \omega)$ 100 times, randomly removing 20% of the cross correlations at each iteration. The resulting set of $\alpha(\omega)$ allowed us to estimate the statistical robustness of the values of attenuation retrieved from the inversion; in this regard, its average approximately coincides with the red curve showed in Figure 12a, with the largest differences being $\sim 2 \times 10^{-7}$ m^{-1} at 0.04 Hz, whereas its standard deviation is at least one order of magnitude smaller than the mean values at all frequencies, varying from 3.18×10^{-7} m^{-1} at 0.3 Hz to 3.42×10^{-8} m^{-1} at 0.04 Hz.

We infer from Figure 12 that our estimates of α, and their dependence on ω, are similar to those found by Patton and Taylor (1984) and Lin (1989) from earthquake-based Rayleigh waves; at the same frequencies, the values proposed by Lawrence and Prieto (2011) based on seismic ambient noise are slightly larger. At higher frequencies (> 0.2 Hz), our measurements fit well those that would be obtained by linearly extrapolating the values of α reported by Lin (1989). At frequencies lower than ~0.065 Hz (periods 16 s), on the contrary, we observe an increase of α, in disagreement with some of the early observations shown in Figure 12.

As shown in Section 4.3, attenuation is significantly underestimated if the distribution of noise sources is limited to the far field of the receivers. If this was the case in the real world, we should observe a significant discrepancy between ambient-noise- and earthquake-based attenuation estimates, the latter being systematically larger than the former. Our estimates, however, are compatible with those obtained from earthquakes by previous authors in the area of interest. This suggests that ambient noise in the frequency range relevant to this study might be generated in the relative vicinity of our receiver array, i.e., within the continent; alternatively, other complex non-homogeneities in the distribution of noise sources might compensate for the lack of sources in the near field. This issue merits further attention, but is beyond the scope of our current study.

6. Conclusions

We have validated numerically the method proposed by Boschi et al. (2019, 2020) to quantify the attenuation of Rayleigh waves from the cross correlation of seismic ambient noise. We achieved this by simulating the displacement associated with 200,000 impulsive sources and recorded by 29 receivers. In all our simulations, we imposed realistic values of phase velocity and attenuation ($\alpha = 5 \times 10^{-7}$ m^{-1}, $\alpha = 1 \times 10^{-6}$ m^{-1}, and a frequency-dependent $\alpha = \alpha(\omega)$ ranging from 3×10^{-7} to 1×10^{-6} m^{-1}). Synthetic data were generated and inverted based on a suite of different setups. We first considered the "ideal" case of a uniform distribution of noise sources; then we implemented three different spatially heterogeneous source distributions: the first characterized by significant azimuthal variations in source density, another by the absence of noise sources in the near field of the receivers, and the third involving rapid source density variations with both distance and azimuth (i.e., a "patchy" source distribution). For each experimental setup, we first verified the cancellation of the "cross terms," predicted by the theory (Equation 4) when the ambient wave field is diffuse and the spectrum of emitted noise does not change as a function of source location; we then verified that the source spectrum is reconstructed accurately, as predicted by the theory, if the source density and attenuation coefficient α are known. Finally, we performed an inversion to measure α from normalized cross correlations of synthetic recordings, through the cost function $C(\alpha, \omega)$. The definition of $C(\alpha, \omega)$ involves a sum over all available station pairs and therefore all available propagation azimuths; importantly, this reduces the unwanted effects of nonuniformities in source distribution. We successfully retrieved the correct values of α in synthetic experiments where noise sources had been deployed in both the near and far field, with good accuracy over a broad frequency range. This result confirms that it is possible to estimate attenuation reliably, even if the assumption of a diffuse wavefield is not exactly met by the data. On the other hand, we inferred from the third experiment that when noise sources are absent from the near field of the receivers both source spectrum and attenuation are significantly underestimated.

Having validated our method by synthetic tests, we compiled a data set of noise recordings using 33 broadband receivers distributed within part of the Colorado plateau and of the Great Basin. We first used this data set to quantify the diffusivity of the ambient wavefield, calculating the signal-to-noise ratio (SNR) as a function of azimuth within the area of interest. The SNR proved to be rather homogeneous in the energy band characteristic of the primary microseisms (centered at the period of 14 s), but revealed a SW-NE preferential directionality of the noise sources within the secondary microseism band (6–8 s); this observation is compatible with what reported in previous studies. When inverting the data to constrain α, the effects of SNR inhomogeneity with respect to azimuth are reduced both by ensemble averaging over time, and implicit averaging over azimuth in the definition of $C(\alpha, \omega)$. The resulting estimates of α, confirmed by a bootstrap analysis, range from $\sim 1 \times 10^{-5}$ m^{-1} at 0.3 Hz to $\sim 4.5 \times 10^{-7}$ m^{-1} at 0.065 Hz; in this frequency range, those values are compatible with previous observations made on the basis of both earthquake-generated and ambient Rayleigh waves.

Data Availability statement

The facilities of IRIS Data Services, and specifically the IRIS Data Management Center (http://ds.iris.edu/ds/nodes/dmc/), were used for access to waveforms, related metadata, and/or derived products used in this study. The authors used publicly available seismic data from the Transportable Array (TA) seismic network (https://doi.org/10.7914/SN/TA).

Acknowledgments
Our many exchanges with Emanuel Kästle, Kees Weemstra, and Sebastian Lauro were very beneficial to this study. The authors are also indebted to two anonymous reviewers for their very careful and insightful reviews. The authors thank the makers of Obspy (Beyreuther et al., 2010). Graphics were created with Python Matplotlib (Hunter, 2007). The Grant to Department of Science, Roma Tre University (MIUR-Italy Dipartimenti di Eccellenza, ARTICOLO 1, COMMI 314-337 LEGGE 232/2016) is gratefully acknowledged.

References

Abramowitz, M., & Stegun, I. A. (1964). *Handbook of mathematical functions*. National Bureau of Standards–Applied Mathematics Series.
Aki, K. (1957). Space and time spectra of stationary waves with special reference to microtremors. *Bulletin of The Earthquake Research Institute, University of Tokyo*, *35*, 415–456.
Al-Khatib, H. H., & Mitchell, B. J. (1991). Upper mantle anelasticity and tectonic evolution of the western United States from surface wave attenuation. *Journal of Geophysical Research*, *96*(B11), 18129–18146.
Asten, M. W. (2006). On bias and noise in passive seismic data from finite circular array data processed using SPAC methods. *Geophysics*, *71*(6), V153–V162.
Bendat, J. S., & Piersol, A. G. (2011). *Random data: Analysis and measurement pocedures* (Vol. 729). John Wiley & Sons.
Bensen, G., Ritzwoller, M., Barmin, M., Levshin, A. L., Lin, F., Moschetti, M., et al. (2007). Processing seismic ambient noise data to obtain reliable broad-band surface wave dispersion measurements. *Geophysical Journal International*, *169*(3), 1239–1260.
Beyreuther, M., Barsch, R., Krischer, L., Megies, T., Behr, Y., & Wassermann, J. (2010). ObsPy: A Python toolbox for seismology. *Seismological Research Letters*, *81*(3), 530–533.
Boschi, L., Magrini, F., Cammarano, F., & van der Meijde, M. (2019). On seismic ambient noise cross-correlation and surface-wave attenuation. *Geophysical Journal International*, *219*(3), 1568–1589.
Boschi, L., Magrini, F., Cammarano, F., & van der Meijde, M. (2020). Erratum: On seismic ambient noise cross-correlation and surface-wave attenuation. *Geophysical Journal International*, *222*(2), 1090–1092.
Boschi, L., & Weemstra, C. (2015). Stationary-phase integrals in the cross-correlation of ambient noise. *Reviews of Geophysics*, *53*, 411–452. https://doi.org/10.1002/2014RG000455
Boschi, L., Weemstra, C., Verbeke, J., Ekström, G., Zunino, A., & Giardini, D. (2013). On measuring surface wave phase velocity from station–station cross-correlation of ambient signal. *Geophysical Journal International*, *192*(1), 346–358.
Campillo, M., & Roux, P. (2014). *Seismic imaging and monitoring with ambient noise correlations*. In B. Romanowic & A. M. Dziewonski (Eds.), *Treatise of geophysics* (Vol. 1, pp. 391–417). Elsevier.
Cupillard, P., & Capdeville, Y. (2010). On the amplitude of surface waves obtained by noise correlation and the capability to recover the attenuation: A numerical approach. *Geophysical Journal International*, *181*(3), 1687–1700.
De Boor, C. (1978). *A practical guide to splines* (Vol. 27). New York: Springer-Verlag.
Ekström, G. (2014). Love and Rayleigh phase-velocity maps, 5–40 s, of the western and central USA from USArray data. *Earth and Planetary Science Letters*, *402*, 42–49.
Ekström, G., Abers, G. A., & Webb, S. C. (2009). Determination of surface-wave phase velocities across USArray from noise and Aki's spectral formulation. *Geophysical Research Letters*, *36*, 1–5. https://doi.org/10.1029/2009GL039131
Friedrich, A., Krüger, F., & Klinge, K. (1998). Ocean-generated microseismic noise located with the Gräfenberg array. *Journal of Seismology*, *2*(1), 47–64.
Hillers, G., Graham, N., Campillo, M., Kedar, S., Landès, M., & Shapiro, N. (2012). Global oceanic microseism sources as seen by seismic arrays and predicted by wave action models. *Geochemistry, Geophysics, Geosystems*, *13*(1).
Hunter, J. D. (2007). Matplotlib: A 2D graphics environment. *Computing in Science & Engineering*, *9*(3), 90–95. https://doi.org/10.1109/MCSE.2007.55
Jones, E., Oliphant, T., Peterson, P., et al. (2001). *SciPy: Open source scientific tools for Python*. Retrieved from http://www.scipy.org/ (Online accessed).
Kästle, E., Soomro, R., Weemstra, C., Boschi, L., & Meier, T. (2016). Two-receiver measurements of phase velocity: Cross-validation of ambient-noise and earthquake-based observations. *Geophysical Journal International*, *207*, 1493–1512.
Kinsler, L. E., Frey, A. R., Coppens, A. B., & Sanders, J. V. (1999). *Fundamentals of acoustics* (4th ed.). Wiley.
Landès, M., Hubans, F., Shapiro, N. M., Paul, A., & Campillo, M. (2010). Origin of deep ocean microseisms by using teleseismic body waves. *Journal of Geophysical Research*, *115*(B5), 1–14.

Lawrence, J. F., & Prieto, G. A. (2011). Attenuation tomography of the western United States from ambient seismic noise. *Journal of Geophysical Research*, *116*(B6), 1–11.

Lehujeur, M., & Chevrot, S. (2020). Eikonal tomography using coherent surface waves extracted from ambient noise by iterative matched filtering–application to the large-N maupasacq array. *Journal of Geophysical Research: Solid Earth*, *125*(6), e2020JB019363. https://doi.org/10.1029/2020JB019363

Lin, W. (1989). *Rayleigh wave attenuation in the Basin and Range province*. St. Louis, MO: St. Louis University.

Menon, R., Gerstoft, P., & Hodgkiss, W. S. (2014). On the apparent attenuation in the spatial coherence estimated from seismic arrays. *Journal of Geophysical Research: Solid Earth*, *119*(4), 3115–3132. https://doi.org/10.1002/2013JB010835

Mitchell, B. J. (1995). Anelastic structure and evolution of the continental crust and upper mantle from seismic surface wave attenuation. *Reviews of Geophysics*, *33*(4), 441–462.

Nakahara, H. (2012). Formulation of the spatial autocorrelation (SPAC) method in dissipative media. *Geophysical Journal International*, *190*(3), 1777–1783.

Patton, H. J., & Taylor, S. R. (1984). Q structure of the basin and range from surface waves. *Journal of Geophysical Research*, *89*(B8), 6929–6940.

Press, W. H., Teukolsky, S. A., Vetterling, W. T., & Flannery, B. P. (1992). *Numerical recipes in fortran* (2nd ed.) Cambridge University Press.

Prieto, G., Lawrence, J., & Beroza, G. (2009). Anelastic earth structure from the coherency of the ambient seismic field. *Journal of Geophysical Research*, *114*(B7), 1–15.

Savitzky, A., & Golay, M. J. (1964). Smoothing and differentiation of data by simplified least squares procedures. *Analytical Chemistry*, *36*(8), 1627–1639.

Tanimoto, T., Ishimaru, S., & Alvizuri, C. (2006). Seasonality in particle motion of microseisms. *Geophysical Journal International*, *166*(1), 253–266.

Tian, Y., & Ritzwoller, M. H. (2015). Directionality of ambient noise on the Juan de Fuca plate: Implications for source locations of the primary and secondary microseisms. *Geophysical Journal International*, *201*(1), 429–443. https://doi.org/10.1093/gji/ggv024

Tsai, V. C. (2011). Understanding the amplitudes of noise correlation measurements. *Journal of Geophysical Research*, *116*(B9), 1–16.

Weemstra, C., Boschi, L., Goertz, A., & Artman, B. (2013). Seismic attenuation from recordings of ambient noise. *Geophysics*, *78*(1), Q1–Q14.

Weemstra, C., Snieder, R., & Boschi, L. (2015). On the estimation of attenuation from the ambient seismic field: Inferences from distributions of isotropic point scatterers. *Geophysical Journal International*, *203*(2), 1054–1071.

Weemstra, C., Westra, W., Snieder, R., & Boschi, L. (2014). On estimating attenuation from the amplitude of the spectrally whitened ambient seismic field. *Geophysical Journal International*, *197*(3), 1770–1788.

Yang, Y., & Ritzwoller, M. H. (2008). Characteristics of ambient seismic noise as a source for surface wave tomography. *Geochemistry, Geophysics, Geosystems*, *9*(2), 1–18.

Yokoi, T., & Margaryan, S. (2008). Consistency of the spatial autocorrelation method with seismic interferometry and its consequence. *Geophysical Prospecting*, *56*(3), 435–451.